Investigation on the seismic response of nuclear power stations with pile-raft foundation in clay using dynamic centrifuge test

Abstract: The research to predict reliably seismic response of the nuclear power station with a pile-raft foundation is required for the high safety requirement of the nuclear power station. In this study, a scaled superstructure with a 4×3 pile-raft foundation, which is constructed in Shanxi kaolin clay, is modelled. Accordingly, the characteristics of seismic response for nuclear power stations with a pile-raft foundation are analyzed using the dynamic centrifuge tests. Especially, multi earthquake motions with different magnitudes and frequency properties are utilized to map the relationship between structural response and properties of earthquake motions. Results show that the seismic response of the soil, raft, and structure are significantly affected by the natural frequency and magnitude of the earthquake motion. The soil surface acceleration is lower than the raft acceleration. The results can provide reliable references for a better understanding of the seismic response of nuclear power stations.

Keywords: dynamic centrifuge test; seismic response; pile-raft foundation; nuclear power station; soil-structure interaction

1. Introduction

Pile foundations have been widely utilized in soft soil areas for various modern structural systems, including buildings, bridges, offshore wind farms, and railway foundations (Chen *et al*. 2011; Katzenbach *et al*. 2016; Wu *et al*. 2017; Zhou *et al*. 2016). As more-sophisticated theoretical and experimental research into the pile foundation, the recognition of raft contribution to the performance of the pile foundation gained acceptance (Bhaduri and Choudhury 2020; Clancy and Randolph 1993; Nguyen *et al*. 2013; Poulos 2001; Roy *et al*. 2018). Considering the state of construction technology development for nuclear power stations and site limitations, only a few such stations have been built around non-rock areas, such as the Clinton, Grand Gulf, River Bend, and Callaway nuclear power stations in the USA. Moreover, no such project has been constructed in China around soft soil areas. The current requirement for nuclear power station sites is that the foundation should rest on firm shallow rock layers (NB/T20308-2014: design code for nuclear safety-related plant foundation for pressure water reactor nuclear power plants). However, the number of sites that satisfy this requirement is limited, and there are other considerations in the decision-making process for the location of nuclear stations. There is little published research on the seismic response of nuclear power stations located in soft soil areas with a pile-raft foundation. Considering the catastrophic loss of life and property to society as caused by earthquakes (Ohnishi 2012), research on the seismic response of such nuclear power stations is urgent.

A pile-raft foundation under earthquake loads is subject to two different forces: inertial forces from the superstructure and ground deformations induced by the seismic load. The dynamic response of the structural system are influenced by ground motion amplification, stiffness differences between the foundation and the soil, and stiffness degradation (Avilés and Pérez-Rocha 1998; Bi *et al*. 2011; Dutta *et al*. 2005; Ghosh and Madabhushi 2007; Kim and Roesset 2004; Moghaddasi *et al*. 2011; Sgarlato *et al*. 2011), which significantly increases the complexity of the problem. When designing pile-raft foundations, the soil, foundation, and superstructure should be considered as an integrated structural system (Boulanger *et al*. 1999; Roy *et al*. 2020; Saha *et al*. 2015); however, the calculation method is not provided in related codes. After earthquakes in Mexico City in 1985, Northridge in 1994, and Kobe in 1995, the post-seismic observations have pushed research focus towards the soil-structure interaction (SSI) effects. Understanding the SSI characteristic seismic response of nuclear power stations with pile-raft foundations in soft soil is critical to ensure their safe operation.

The dynamic Centrifuge test is a useful tool to study the seismic response of structures while considering the SSI effect. However, sands are typically used instead of clays (Baziar *et al*. 2018; Sawada and Takemura 2014; Wilson *et al*. 2000; Yoo *et al*. 2017). A single pile-structure system was studied without considering the pile group effect (Boulanger *et al*. 1999), and a shallow foundation (but not a pile foundation) was used (Ghosh and Madabhushi 2007; Trombetta *et al*. 2013). Also, the structure loads were usually simplified as a mass block (Banerjee *et al*. 2014; Hussien *et al*. 2016; Liang *et al*. 2020; Zhang *et al*. 2017). For nuclear power stations, the dynamic centrifuge model cannot be oversimplified due to the associated safety requirements.

In this paper, the seismic response of a nuclear power station was studied using dynamic centrifuge model tests with a 50 g gravity level. The scaled superstructure with a 4×3 pile-raft foundation was constructed in Shanxi kaolin clay and was subjected to different earthquake shaking types and magnitudes. The soil, raft, and structural accelerations, the pore water pressure of the clay soil, the bending moment of typical piles, the container's horizontal displacement, and the structure's displacements were recorded. This paper reports the seismic response of nuclear power stations with an emphasis on the structural acceleration and pile bending moment. This research provides a reference to understand the seismic response of nuclear power stations.

2. Dynamic Centrifuge Test Set-up

The dynamic centrifuge tests were performed at Tongji University using the TLJ-150 geotechnical centrifuge (Liang *et al*. 2020), as shown in Figure 1. The frequency of the excitation ranges from 20 to 200 Hz. The maximum dynamic centrifuge acceleration is 50 g, and the maximum shaking duration under the maximum acceleration is 1 s. The laminar shear model box is shown in Figure 2.

2.1 The Dynamic Centrifuge Model

The nuclear power station model was designed according to the third-generation nuclear power station in China. Due to the limited capability of the centrifuge shaking table, the prototype dimension of the scaled model in the tests is about 10 times smaller than the practical project structure. Note that the dimensions of the structure and test results in this study are presented for the prototype unless otherwise stated. The superstructure mainly includes a containment structure for the nuclear reactor (cylinder and dome) and a cuboid annex for the reactor, and the corresponding model is shown in Figure 3. The scaling laws for the dynamic centrifuge testing are illustrated in Table 1(Ghosh *et al.*, 2007). The properties of the model and prototype are summarized in Table 2. The length, width, height, and thickness of the cuboid are 11.05 m, 8.20 m, 3.70 m, and 0.05 m, respectively. The reactor can be divided into two parts, including the cylinder and dome. In particular, the height, diameter, and thickness of the cylinder are 6.09 m, 5.40 m, and 0.1 m, respectively. The height and thickness of the dome are 1.12 m and 1.25 m, respectively. Besides, the cuboid of the model is made of polymethyl methacrylate (PMMA) with a density of 1.18 g/cm^3. The material of the raft and cylinder is aluminium. The dome is made of iron with a density of 7.8×10^3 kg/m^3.

The length, width, and height of the internal space in the laminar shear model box utilized in the test are 25 m, 20 m, and 27.5 m, respectively. The box consists of 22 high-strength hollow aluminium rings (each with a height of 1.25 m). Also, an inside rubber membrane, which is used to minimize the effects of boundary reflections, is mounted on the internal surface of the aluminium rings. Hence, the boundary effect of the box is negligible (Yang *et al*. 2019). Besides, four drainage holes at the bottom corner are covered with permeable stones, as shown in Figure 2. The drainage holes create a double-sided drainage consolidation environment.

The model and corresponding sensor layout are shown in Figure 4. The length, width, and height of the raft are 11.9 m, 9.05 m, and 0.8 m, respectively, and the distance between the raft edge and the external cuboid edge is 0.43 m. The length, diameter, and thickness of the tube pile are 15 m, 0.7 m, and 0.05 m, respectively. The tube pile is made of aluminium with a density of 2.7 g/cm^3. The properties of the piles are shown in Table 3, compared with the piles in three previous studies(Boulanger *et al*. 1999; Yang *et al*. 2019; Zhang *et al*. 2017). Note that the test results in these studies are also presented in the following.

As shown in Figure 4, the clay depth at Shanxi kaolin is 17.5 m. Under the clay, there is a 2.5 m thick sand layer that acted as a filter layer. The shaking direction is along the short edge (width) of the raft, and the model has axial symmetry. There were 12 piles in this work that were rigidly fixed to the raft using bolts with a pile spacing of 2.24 m, which is three times the pile diameter. Three piles, named P-1, P-2, and P-3, in the pile-raft foundation were equipped with four full-bridge strain gauges to determine the bending moment of the piles. The relationship between the strain and bending moment in each sensor position of the piles was calibrated via step-by-step loading based on a cantilever beam. Four accelerometers were arranged at various locations and utilized to measure the seismic acceleration of the soil at depths of 20 m (A4) and 1 m (A3) and at the raft (A2) and structure (A1). Note that recorded data via A4 and A3 were the input motion and soil surface acceleration, respectively. Six displacement transformers (LS1–LS3 and DS1–DS3) were used to scan the time history of the model displacement and the soil box. The LS1 and LS2 were equipped at different sides of the structure, measuring the settlement and inclination. LS1 and LS2 were placed near the edge of the structure at a distance of 1.25 m apart. The LS3 was installed to measure the horizontal displacement of the structure under seismic loading. Three differential displacement meters were equipped along the shaking direction at the side of the laminar shear model box to measure the horizontal displacement of the soil under seismic loading at the 7th, 11th and 16th high-strength hollow aluminium rings.

A sand layer with a thickness of 2.5 m was first paved into the base of the model box. The sand used at the bottom of the box was Fujian standard sand with diameters ranging from 0.5 mm to 1 mm. The filter paper was then paved on the surface of the sand, above which the kaolin clay was poured. The clay beds used in the centrifuge model tests were prepared using Shanxi kaolin powder. The kaolin clay powder and water mixture (2:1) were subjected to 24 h of preloading under 1 g conditions with double drainage. There were four drainage holes at the perimeter connected with internal permeable stone at the bottom. This configuration is beneficial to implement double-sided drainage consolidation for soft clay. Lastly, another filter layer was placed on the

surface of the kaolin clay, and 25 kg of sand was loaded on the filter. The sand corresponded to effective overburden stress of approximately 1.23 kPa at the top of the clay mixture.

The box was loaded onto the shaking table of the centrifuge to perform centrifuge consolidation under a 50 g gravity field to develop the required strength profile and stress history under double-sided drainage conditions. To accurately control this process, a laser displacement sensor was applied to measure the soil surface settlement, while a pore water pressure sensor (B1) monitored the dissipation of the excess pore water in the soil. After 20 h, the soil settlement rate was reduced, and the pore water pressure tended to stabilize; thus, the centrifuge consolidation was considered to be complete. The top sand layer and filter paper were removed after in-flight centrifuge consolidation of the clay was completed. The basic properties of the Shanxi kaolin clay used in this study are shown in Table 4. The water content was tested after the dynamic centrifuge tests were completed.

2.2 Ground Motion

The dynamic centrifuge tests were performed with three ground motions and white noise. The ground motions used in the tests included two natural earthquake waves and an artificial seismic wave. In particular, 1940 El Centro wave (EL) and 1985 Mexico City wave (MEX) are the two selected natural earthquake waves. The YG seismic wave is an artificial seismic wave based on the EUR soft design response spectrum, in case the model may build in soft area. According to the centrifuge test scaling ratio and the excitation frequency (20 Hz to 200 Hz) of the shaker, the earthquake waves are scaled in time and amplitude using a Butterworth bandpass filter. The acceleration and Fourier amplitude of the selected earthquake waves with a peak acceleration of 0.1 g is shown in Figure 5. The duration and predominant period of the YG wave are 25 s and 0.35 s (corresponding predominant frequency, 2.88 Hz), respectively. The duration of the EL wave and MEX wave is 50 s. However, the predominant periods of the EL wave and MEX wave are 0.41 s (corresponding predominant frequency, 2.43 Hz) and 2.22 s (corresponding predominant frequency, 0.45 Hz), respectively. The EL wave and MEX wave represent short period and long period ground motions, respectively. The white noise excitation is conducted at the beginning of the tests with frequency ranging from 20 Hz to 200 Hz to determine the dynamic characteristics of the test model using transfer function.

2.3 Test Schedule

Three ground motions, including the YG, EL, and MEX, and a white noise are adopted as input excitation. The YG and EL are applied at three magnitudes, including 0.1 g, 0.2 g, and 0.3 g. In addition, the magnitudes of the MEX and white noise are 0.1 g and 0.05 g, respectively.

The actual acceleration acting on the shaking table significantly depends on the methods of wave generation, mainly including the peak ground acceleration-based method (PGA-based method) and energy-control method. The energy-control method, which controls the energy of the input excitation, is utilized in this study. An accelerometer, A4, is mounted on the shaking table, aiming at recording the actual excitation. Eight test cases are illustrated in Table 5. The α_{max} is the designed magnitude of input ground motions, and the A_{max} represents the actual magnitude of the input excitation, which is recorded by the accelerometer, A4. The main test procedures for the dynamic centrifuge tests are shown as follows.

(i) The strain gauges are mounted on the piles and connect to the data acquisition using the full-bridge circuit. The gauge wires are placed in the tubular pile through a pre-punched hole. Two different protection types of glue, including the silica gel and epoxy resin, are used to make the structure waterproof. Afterward, the strain gauges are connected to the data acquisition using the gauge wires.

(ii) The soil sample is paved into the box. After the consolidation of the soil sample, the box is mounted on the shaking table to determine the best operating voltage for all input motions. The operating voltage for the driver is determined based on the correlation between the input signal and the output acceleration.

(iii) The positioning device is established to ensure the installation accuracy of piles.

(iv) The displacement transformers and acceleration sensors are mounted on the raft and structure. Afterward, the box, in which the test model and soil sample are installed, is mounted on the shaking table.

(v) Based on the best operating voltage, the dynamic centrifuge tests with different excitations are conducted orderly.

3. Test Results and Discussion

3.1 Dynamic characteristics of the model

The seismic response of the model under white noise excitation was first studied to analyze the dynamic characteristics of the model. The time history acceleration and the Fourier amplitude spectra under the white noise excitation were shown in Figure 6. Time history acceleration curves at the soil depth of 20 m, at the soil depth of 1 m, of the raft foundation and the structure were shown in Figure 6(a). The maximum acceleration of the soil during the tests at a depth of 20 m (input motion) and 1 m (soil surface) and at the raft and structure were 0.07 g, 0.08 g, 0.08 g and 0.10 g, respectively, as shown in Figure 6(a). The objective input motion magnitude was 0.05 g; however, the practical input motion recorded by A4 at the depth of 20 m was 0.07 g. Figure 6(b) shows the Fourier amplitude spectra of the acceleration for this test. It can be seen that the low-frequency component is distributed over most of the frequency ranges. The dominant frequencies for the soil at a depth of 20 m and the soil at a depth of 1m are 3.45 Hz and 1.20 Hz, respectively, and the peak values for the raft and structure are 1.20 Hz and 2.70 Hz, respectively. There are two peak values, as illustrated in Figure 6(b) for the structure, 1.21 Hz, and 2.70 Hz. The seismic response of the structure and the raft are different.

Since the Fourier spectra of the shaking table acceleration is $F(w)$ and that of raft, structure, and soil at a depth of 1 m is $G(w)$, the transfer function $H(w)$ of the raft, structure and soil acceleration is given by $H(w) = G(w)/F(w)$ (Liang *et al.* 2019). As shown in Figure 7, the transfer functions $H(w)$ of the surface soil and the raft are similar, showing one dominant peak at 1.31 Hz and a secondary peak at 2.84 Hz in each transfer function. The dominant peak frequency for the structure is smaller at 1.29 Hz. Besides, there is no secondary peak at the high-frequency range, which is because of the dynamic characteristics of the superstructure.

3.2 Influence of input motion and peak base acceleration on the response of soil and structure

After White noise excitation, seven other tests were performed independently, as shown in Table 5. Figure 8 shows the recorded acceleration and the Fourier spectra under 0.1 g, 0.2 g, and 0.3 g YG wave excitations. Under 0.1 g YG wave excitation, the maximum acceleration at a soil depth of 20 m (input motion), at the soil depth of 1 m, the raft and structure were 0.15 g, 0.13 g, 0.24 g, and 0.38 g, respectively, as shown in Figure 8(a). The dominant frequencies at those locations were 1.73 Hz, 0.98 Hz, 1.69 Hz, and 1.71 Hz, as shown in Figure 8(b). The dominant frequency at the surface of the soil (soil depth=1 m) was lower than that at the soil depth of 20 m. This implied that the high-frequency of the input motion was depressed, and the low-frequency component was enlarged. The same characteristic was shown with 0.2 g and 0.3 g YG wave excitation, as shown in Figures 8(c) to 8(f). Figures 9 and 10 show the recorded acceleration and Fourier spectra under the EL and MEX excitations, respectively.

The peak accelerations of input motion, soil surface, raft, and structure were shown in Figures 8 to 10 for each of the seven tests. These comparisons are summarised in Figure 11. The peak acceleration of soil surface, raft, and structure increased with the increase of input motion magnitude. The response of structure and raft under the YG excitation was weaker than that under the EL excitation. For example, under 0.2 g YG wave and EL wave excitation, the peak accelerations of the structure were 0.40 g and 0.47 g, respectively. The peak acceleration of soil surface, raft, and structure response were strongly affected by the frequency content of the earthquake motion (i.e., YG versus EL) as well as by the level of shaking. The frequency content of the earthquakes was illustrated in Figure 5, which shows the Fourier amplitude spectra for the base input motions with the same peak accelerations. The YG input motions had smaller spectral accelerations than the EL input motions in the frequency range from 1 to 3 Hz. This was the main reason why the soil, raft, and structural models under YG excitation responded less strongly than the EL excitation.

The peak accelerations of the soil surface, raft, and structure over the peak acceleration of the input motions were calculated to determine the amplification ratios, as shown in Figure 12. The amplification ratios generally decrease with a more significant base peak acceleration. This trend is consistent with the expected effects of nonlinearity for the ranges of structural periods, soil profile periods, and input frequency content for these tests. As seen from the results of the YG-0.1 g, YG-0.2 g, and YG-0.3 g cases, the amplification ratios of the structure are 2.61, 1.53, and 1.21, respectively. The same principle is generated for the EL-0.1 g, EL-0.2 g, and EL-0.3 g cases. Similar results were obtained from the previous research (Boulanger *et al*. 1999; Liang *et al*. 2017; Liu *et al*. 2018). However, the results were in contrast with the previous findings (Ghosh and Madabhushi, 2007), which concluded that using the free surface motion as the foundation input motion in design could be a conservative approximation in many soil profiles with a similar layering. The acceleration of the raft, in this study, was higher than that on the soil surface, because the raft bears the load transferred from the foundation and the inertial forces from the structure under dynamic loads.

3.3 Influence of soil depth and input motion on the horizontal displacement of soil

Three displacement meters, DS-1, DS-2, and DS-3 were located on the side of the laminar shear model box at the 7th, 11th, and 16th high-strength hollow aluminium rings. The soil depth at the 7th, 11th, and 16th rings are 1 m, 5.8 m, and 11.8 m, respectively. The recorded horizontal displacements of the soil under the YG wave, the EL wave, and the MEX wave excitations are shown in Figure 13. The maximum horizontal displacements for each earthquake excitation obtained from Figure 13 were summarised in Table 6 and Figure 14. The horizontal displacement of the soil at a deeper depth had a more significant horizontal displacement because of the reduction effect of clay. For example, under the YG-0.1 g excitation, the peak horizontal displacement of the soil at the depth of 1 m, 5.8 m, and 11.8 m were 35.33 mm, 48.09 mm, and 64.71 mm, respectively. This amplifying characteristic was the same for all the other cases and was caused by the properties of the clay. The peak horizontal displacement of the soil increased with the increase of the magnitude of earthquake waves. The peak horizontal displacement of the soil under the MEX wave was the largest at comparable input magnitudes. This may be because a dominant frequency (1.31 Hz) generated from the transfer function of the soil at the depth of 1 m is, as shown in Fig.8, closer to the second dominant frequency (1.42 Hz) of the input MEX waves, as shown in Figure 10(b), which induces a resonance effect.

3.4 Influence of input motion and peak base acceleration on the excess Pore Water Pressure

A piezometer was located at the bottom of the box to record the excess pore water pressure of the soil under the earthquake wave excitation. The original pore water pressure was zero as caused by the reset operation of the acquisition system, so the recorded pore water pressure data by piezometer was the excess pore water pressure.

Figure 15 shows the excess pore water pressure under all considered earthquake wave excitations. Figure 15(a) shows the excess water pressure under the YG wave excitations, including 0.1 g, 0.2 g, and 0.3 g. The excess pore water pressure increased with the increase of input motion magnitude. The same characteristic was shown in Figure 15(b) under the EL wave excitation. Note that the instant peak excess pore water pressure under the EL-0.2 g case was higher than that under the EL-0.3 g case because of the practical input motion peak acceleration for the EL-0.2 g case and EL-0.3 g case were 0.24 g and 0.23 g, respectively. For the MEX-0.1 g case, the excess pore water pressure was higher than the comparable magnitude of input motion, which was induced by the resonance effect as mentioned, as shown in Figure 15(c). After shaking, the pore water pressure appeared to remain stable, implying that much more time was required to reduce the excess pore water pressure for larger acceleration magnitudes.

Figure 16 shows the relationship between peak instant pore water pressure and the magnitude of input motion. The peak excess pore water pressure increases with the acceleration magnitude.

3.5 Influence of input motion on the movement of structure

Under earthquake excitation, the inertial forces generated in the superstructure cause it to rock. This creates horizontal displacements in the structure along with vertical displacements. Three displacement sensors, including LS1, LS2, and LS3, were equipped in the test model to monitor the movement of the structure. For monitoring the vertical displacements, LS1 and LS2 were located at the long edge of the structure with a distance of 9.40 m, as shown in Figure 4. Table 7 shows the vertical displacement and inclination of structure. The vertical displacement at different sides (LS1, LS2) differs because of the rocking, suggesting one side of the foundation has settlement while the other side possibly generates an uplift problem (Hokmabadi and Fatahi, 2016). The maximum plus vertical displacement is 3.7 mm under the excitation of YG-0.3 g, and the maximum minus value is -1.64 mm under the excitation of EL-0.1 g. The maximum average values of LS1 and LS2 is 3.35 mm. Dividing the difference vertical displacement between LS1 and LS2 by their distance 9.4 m was the inclination value. It was utilized to analyze the inclination of the structure, as shown in Table 7. All the incline data for the nuclear power station were acceptable.

In order to monitor the horizontal displacement of the structure, a displacement sensor LS3 was equipped at the side of the structure model, as shown in Figure 4. The cuboid, made from PMMA, is soft generating vibration of itself, which results in the error of horizontal displacement of the structure during earthquake excitation. The residual horizontal displacement after shaking was utilized to analyze the horizontal displacement of the structure. The residual horizontal displacements include the horizontal displacement of the soil and the absolute displacement of the structure. The residual horizontal displacement is shown in Table 8. It is noted that the residual displacement under the MEX-0.1 g earthquake loads is 26.57 mm, which is the largest because of the resonance effect. The horizontal displacement for the YG cases is lower than the EL cases. For example, under the YG-0.3 g case and the EL-0.3 g case, the horizontal displacements of the structure are 13.58 mm and 25.11 mm, respectively.

3.6 Influence of the input motion and pile location on the bending moment of the pile

As shown in Figure 4, three piles (P-1, P-2, and P-3) were equipped with strain gauges to determine the bending moment of the piles. The distance between the first strain gauge and the pile head (bottom of the raft) was 2.5 m. The other three strain gauges were located at the pile depth of 5.0 m, 7.5 m, and 10.0 m, respectively.

The dynamic bending moments of the pile, P-2, under different seismic wave loads, are shown in Figures 17 to 19, respectively. The peak positive and negative moments are labelled in those figures. It is noted that the maximum bending moment is an average of the positive and negative peak bending moments. The values recorded at a pile depth 2.5 m is the maximum along with the pile. This is for enduring the tremendous inertial forces transformed from the superstructure. The frequencies corresponding to the dominant peak of the piles at a 2.5 m depth for the YG-0.1 g, EL-0.1 g, and MEX-0.1 g are 0.27, 1.21, and 0.51 Hz, respectively. The vibration characteristics of the superstructure under different earthquake excitations may cause the dominant peak variety of pile bending moment. Figure 19 shows the pile bending moment under the MEX-0.1 g case, which is different from that under the YG case. During the excitations, the low-frequency MEX wave induced a resonance with the foundation, which caused the bending moments of the piles to increase distinctly.

The pile bending moments for P-2 under the 0.3 g seismic waves were studied, as shown in Figures 20 and 21. The increased wave energy carried under a 0.3 g magnitude caused the maximum Fourier amplitude of pile 2 at a depth of 2.5 m under YG-0.3 g and EL-0.3 g to occur at 0.91 Hz and 0.82 Hz, respectively. The Fourier amplitudes for the same pile decreased at greater depths, as shown in Figures 17 to 21. This was thought to be caused by a decreased pile bending moment with greater depths.

In order to better understand the bending moment of the piles at different depths and locations, the maximum bending moments were determined from the recorded time history bending moment data. Figure 22 shows the maximum bending moment for all piles (P-1, P-2, and P-3). The maximum bending moment decreases with depth and is located primarily at the depth of the 2.5 m. The bending moment of P-2 and P-1 is higher than P-3

because they absorb more earthquake energy and act as a shield for P-3 in the second row. Figure 23 shows the maximum bending moment of the pile at the depth of 2.5 m under different cases. The bending moment for P-3 decreases rapidly compared with the other two piles. The bending moment increases with the input acceleration magnitude, such as for the YG seismic waves at 0.1 g, 0.2 g, and 0.3 g accelerations showing increasing recorded bending moments. It is noted that the maximum pile bending moment at 2.5 m depth under the MEX seismic load is larger than the other seismic loads under the same acceleration magnitude, which is because of the resonance effect.

The amplification or decreased ratio of the maximum pile bending moment was calculated by the ratio of the bending moment of pile heads. P1, P2, and P3 represent the bending moment of pile head for piles located at the corner, at the edge of the second row, and the inner of the second row, respectively. Figure 24 shows the amplification ratio of the maximum pile bending moment of P1/P2. Three research results are shown in Figure 24, including the results in this paper and the previous research results (Yang *et al*. 2019; Zhang *et al*. 2017). Earthquake events 1-6 represent different tests carried out by the researchers. The amplification ratio for pile 1 over pile 2 is approximately 1.5. Attention must be given to ensure the stiffness of the corner piles for it bearing more inertial force transferred from the superstructure and kinematic forces. The decrease ratio in the previous research (Yang *et al*. 2019) was slightly higher than that in this paper. This may be because of the different pile diameter, spacing, and PGA. For the conservative reason, the decrease ratio can be taken as 0.8. The amplification ratio and decrease ratio is only suitable for estimating the bending moment in dynamic centrifuge test and more research is need to take the ratios to practice projects. This paper provides reinforcing evidence of adopting reduced stiffness for the inner pile in design, which brings a financial benefit to such construction projects.

4. Conclusions

In this study, the results of a series of dynamic centrifuge model tests for a nuclear power station on Shanxi kaolin clay, considering the SSI effect, were presented. The following conclusions can be drawn from this study.

(1) The soil acceleration, raft acceleration, and structural acceleration were magnified with various degrees under different intensity excitation. The seismic response of the soil, raft, and structure were strongly affected by the frequency content of the earthquake motion. With the increase of peak base acceleration, the acceleration amplification ratio generally decreased. In the structure design process, the foundation input motion could be different from the soil surface acceleration. The soil near-surface acceleration was lower than the raft acceleration based on the recorded data in this study.

(2) The horizontal displacement of the soil was higher when the frequency of the input motion was in line with the natural frequency of the soil. The instantaneous excess pore water pressure increased with the acceleration magnitude, and more time was required to reduce the excess pore water pressure at larger acceleration magnitudes. Considering the SSI effect, the inertial forces generated from the superstructure resulted in a rocking motion of the structure under earthquake loads, which induced a horizontal displacement of the structure and an uneven soil settlement. Moreover, the pile-raft foundation could endure soil settlement with an acceptable inclination of the raft.

(3) The Fourier amplitudes for the same pile decreased with the depth. At greater depths, the bending moment of the piles decreased but was the largest at the pile head. The first row of the pile group absorbed more earthquake energy and acted as a shield for piles in the second row. This study provided reinforcing evidence of adopting reduced stiffness for the inner pile in design.

References

Avilés, J., Pérez-Rocha, L.E., 1998. Site effects and soil-structure interaction in the valley of Mexico. Soil Dyn. Earthq. Eng. 17, 29-39. https://doi.org/10.1016/S0267-7261(97)00027-4

Banerjee, S., Goh, S.H., Lee, F.H., 2014. Earthquake-induced bending moment in fixed-head piles in soft clay. Géotechnique 64(6), 431-446. https://doi.org/10.1680/geot.12.P.195

Baziar, M.H., Shahnazari, H., Kazemi, M., 2018. Mitigation of surface impact loading effects on the underground structures with geofoam barrier: Centrifuge modeling. Tunn. Undergr. Sp. Technol. 80, 128-142. https://doi.org/10.1016/j.tust.2018.06.010

Bhaduri, A., Choudhury, D., 2020. Serviceability-based finite-element approach on analyzing combined pile-raft foundation. Int. J. Geomech. 20(2), 04019178. https://doi.org/10.1061/(ASCE)GM.1943-5622.0001580

Bi, K.M., Hao, H., Chouw, N., 2011. Influence of ground motion spatial variation, site condition and SSI on the required separation distances of bridge structures to avoid seismic pounding. Earthq. Eng. Struct. Dyn. 40, 1027-1043. https://doi.org/10.1002/eqe.1076

Boulanger, R.W., Curras, C.J., Kutter, B.L., Wilson, D.W., Abghari, A., 1999. Seismic soil-pile-structure interaction experiments and analyses. J. Geotech. Geoenvironmental Eng. 125, 750-759. https://doi.org/10.1061/(ASCE)1090-0241(1999)125:9(750)

Chen, S.L., Song, C.Y., Chen, L.Z., 2011. Two-pile interaction factor revisited. Can. Geotech. J. 48, 754-766. https://doi.org/10.1139/t10-095

Dutta, S.C., Das, P.K., Roy, R., 2005. Seismic behavior of code-designed bidirectionally eccentric systems. J. Struct. Eng. 131, 1497-1514. https://doi.org/10.1061/(ASCE)0733-9445(2005)131:10(1497)

Ghosh, B., Madabhushi, S.P.G., 2007. Centrifuge modelling of seismic soil structure interaction effects. Nucl. Eng. Des. 237, 887-896. https://doi.org/10.1016/j.nucengdes.2006.09.027

Hokmabadi, A.S., Fatahi, B., 2016. Influence of foundation type on seismic performance of buildings considering soil-structure interaction. Int. J. Struct. Stab. Dyn. 16, 1-29. https://doi.org/10.1142/S0219455415500431

Hussien, M.N., Tobita, T., Iai, S., Karray, M., 2016. Soil-pile-structure kinematic and inertial interaction observed in geotechnical centrifuge experiments. Soil Dyn. Earthq. Eng. 89, 75-84. https://doi.org/10.1016/j.soildyn.2016.08.002

Katzenbach, R., Leppla, S., Choudhury, D., 2016. Foundation systems for high-rise structures. CRC press.

Kim, Y.S., Roesset, J.M., 2004. Effect of nonlinear soil behavior on inelastic seismic response of a structure. Int. J. Geomech. 4, 104-114. https://doi.org/10.1061/(ASCE)1532-3641(2004)4:2(104)

Liang, F.Y., Jia, Y.J., Sun, L.M., Xie, W., Chen, H.B., 2017. Seismic response of pile groups supporting long-span cable-stayed bridge subjected to multi-support excitations. Soil Dyn. Earthq. Eng. 101, 182-203. https://doi.org/10.1016/j.soildyn.2017.07.019

Liang, F.Y., Jia, Y.J., Xie, W., Sun, L.M., Chen, H.B., 2019. Transverse response of pile group foundations supporting a long-span cable-stayed bridge under uniform and nonuniform excitation. Soil Dyn. Earthq. Eng. 121, 57-74. https://doi.org/10.1016/j.soildyn.2019.03.002

Liang, F.Y., Liang, X., Zhang, H., Wang, C., Asce, A.M., 2020. Seismic response from centrifuge model tests of a scoured bridge with a pile-group foundation. J. Bridge Eng. 25, 1-13. https://doi.org/10.1061/(ASCE)BE.1943-5592.0001594

Liu, X., Wang, R., Zhang, J.M., 2018. Centrifuge shaking table tests on 4 × 4 pile groups in liquefiable ground. Acta Geotech. 13, 1405-1418. https://doi.org/10.1007/s11440-018-0699-5

Moghaddasi, M., Cubrinovski, M., Chase, J.G., Pampanin, S., Carr, A., 2011. Probabilistic evaluation of soil-foundation-structure interaction effects on seismic structural response. Earthq. Eng. Struct. Dyn. 40, 135-154. https://doi.org/10.1002/eqe.1011

Nguyen, D.D.C., Jo, S.B., Kim, D.S., 2013. Design method of piled-raft foundations under vertical load considering interaction effects. Comput. Geotech. 47, 16-27. https://doi.org/10.1016/j.compgeo.2012.06.007

Ohnishi, T., 2012. The disaster at Japan's Fukushima-Daiichi nuclear power plant after the March 11, 2011 earthquake and tsunami, and the resulting spread of radioisotope contamination. Radiat. Res. 177, 1-14. https://doi.org/10.1667/RR2830.1

P. Clancy, M.F.R., 1993. An approximate analysis procedure for piled raft foundations. Int. J. Numer. Anal. Methods Geomech. 17, 849-869.

Poulos, H.G., 2001. Piled raft foundations: Design and applications. Geotechnique 51, 95-113. https://doi.org/10.1680/geot.51.2.95.40292

Roy, J., Kumar, A., Choudhury, D., 2018. Natural frequencies of piled raft foundation including superstructure effect. Soil Dyn. Earthq. Eng. 112, 69-75. https://doi.org/10.1016/j.soildyn.2018.04.048

Roy, J., Kumar, A., Choudhury, D., 2020. Pseudostatic approach to analyze combined pile–raft foundation. Int. J. Geomech. 20(10), 06020028. https://doi.org/10.1061/(ASCE)GM.1943-5622.0001806

Saha, R., Haldar, S., Dutta, S.C., 2015. Influence of dynamic soil-pile raft-structure interaction: an experimental approach. Earthq. Eng. Eng. Vib. 14(4), 625-645. https://doi.org/10.1007/s11803-015-0050-1

Sawada, K., Takemura, J., 2014. Centrifuge model tests on piled raft foundation in sand subjected to lateral and moment loads. Soils Found. 54(2), 126-140. https://doi.org/10.1016/j.sandf.2014.02.005

Sgarlato, G., Lombardo, G., Rigano, R., 2011. Evaluation of seismic site response nearby underground cavities using earthquake and ambient noise recordings: A case study in Catania area. Italy. Eng. Geol. 122, 281–291. https://doi.org/10.1016/j.enggeo.2011.06.002

Trombetta, N.W., Mason, H.B., Hutchinson, T.C., Zupan, J.D., Bray, J.D., Kutter, B.L., 2014. Nonlinear soil-foundation-structure and structure-soil-structure interaction: centrifuge test observations. J. Geotech. Geoenvironmental Eng. 140(5), 04013057. https://doi.org/10.1061/(ASCE)GT.1943-5606.0001074

Wilson, D.W., Boulanger, R.W., Kutter, B.L., 2000. Observed seismic lateral resistance of liquefying sand. J. Geotech. Geoenvironmental Eng. 126(10), 898-906. https://doi.org/10.1061/(ASCE)1090-0241(2000)126:10(898)

Wu, W., El Naggar, M.H., Abdlrahem, M., Mei, G., Wang, K., 2017. New interaction model for vertical dynamic response of pipe piles considering soil plug effect. Can. Geotech. J. 54(7), 987-1001. https://doi.org/10.1139/cgj-2016-0309

Yang, J., Yang, M., Chen, H.B., 2019. Influence of pile spacing on seismic response of piled raft in soft clay: centrifuge modeling. Earthq. Eng. Eng. Vib. 18(4), 719-733. https://doi.org/10.1007/s11803-019-0532-7

Yoo, M.T., Han, J.T., Choi, J.I., Kwon, S.Y., 2017. Development of predicting method for dynamic pile behavior by using centrifuge tests considering the kinematic load effect. Bull. Earthq. Eng. 15(3), 967–989. https://doi.org/10.1007/s10518-016-9998-0

Zhang, L., Goh, S.H., Yi, J., 2017. A centrifuge study of the seismic response of pile-raft systems embedded in soft clay. Geotechnique 67(6), 479-490. https://doi.org/10.1680/jgeot.15.P.099

Zhou, M., Liu, H.L., Chen, Y.M., Hu, Y.X., 2016. First application of cast-in-place concrete large-diameter pipe (PCC) pile-reinforced railway foundation: A field study. Can. Geotech. J. 53(4), 708-716. https://doi.org/10.1139/cgj-2014-0547

Figures

Figure 1 Photograph of the TLJ-150 geotechnical centrifuge.

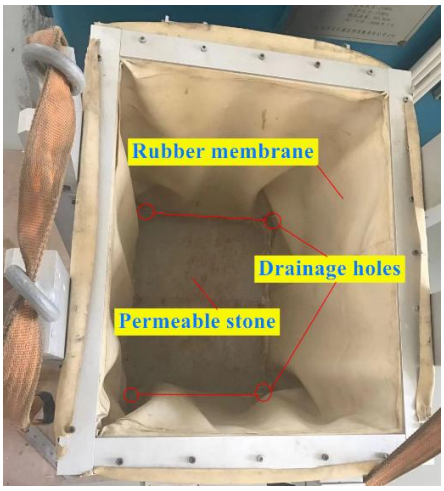

Figure 2 Photograph of the laminar shear model box.

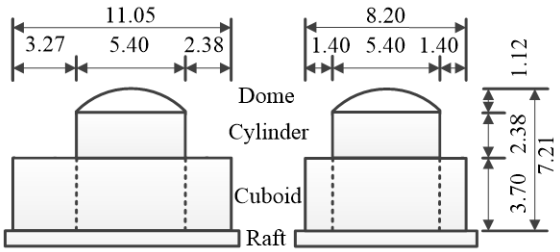

(a) Front view (b) Side view

Figure 3 Schematic for the superstructure model (Unit: m).

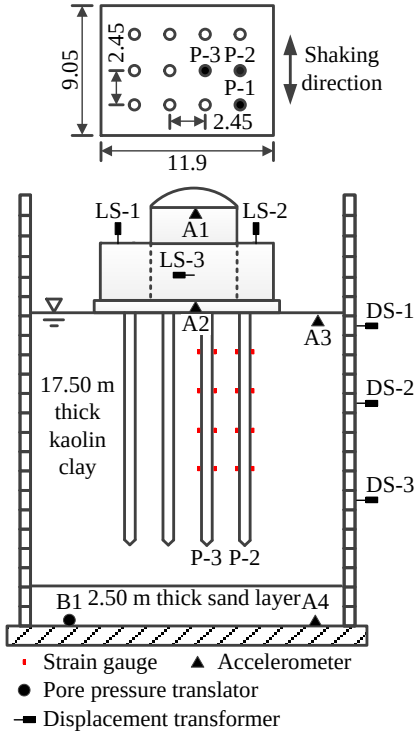

Figure 4 Schematic for the model set-up and sensor locations.

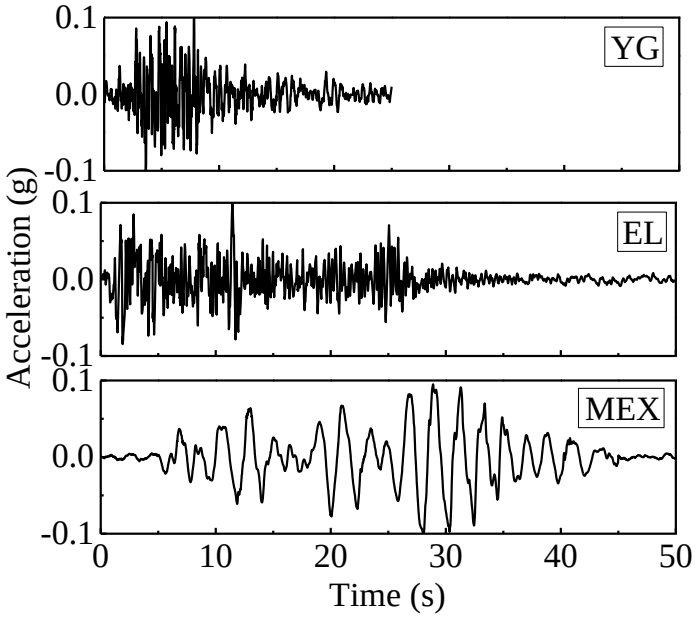

(a) Acceleration

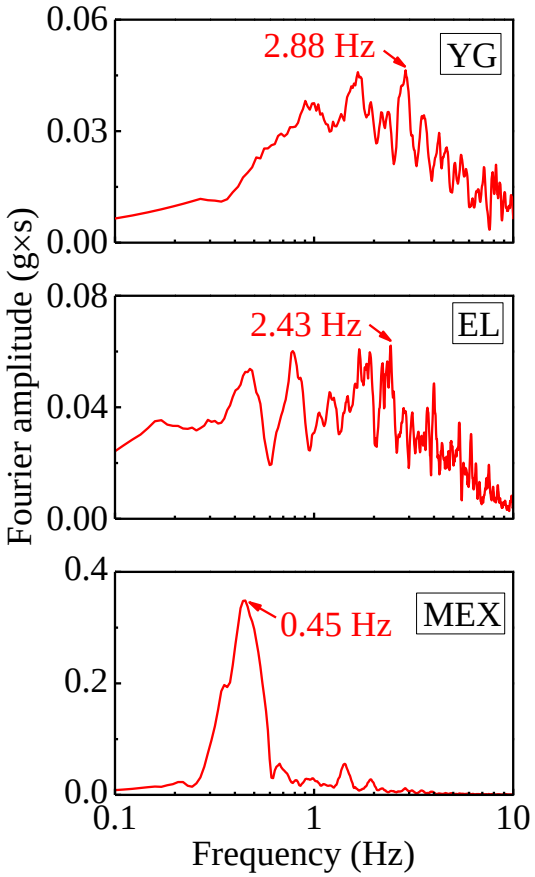

(b) Fourier amplitude spectra

Figure 5 Input seismic waves used in the dynamic centrifuge tests.

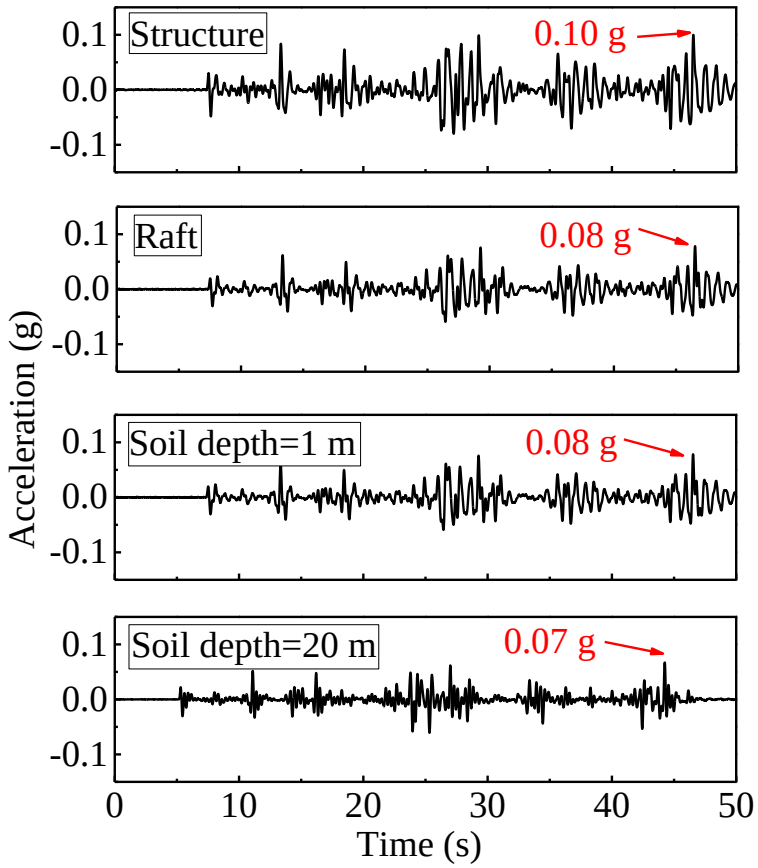

(a) Acceleration time history

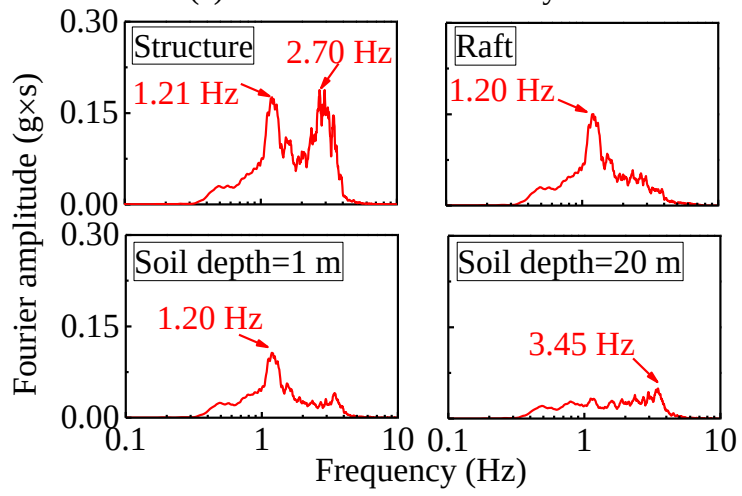

(b) Fourier amplitude spectra

Figure 6 Measured acceleration under white noise excitation.

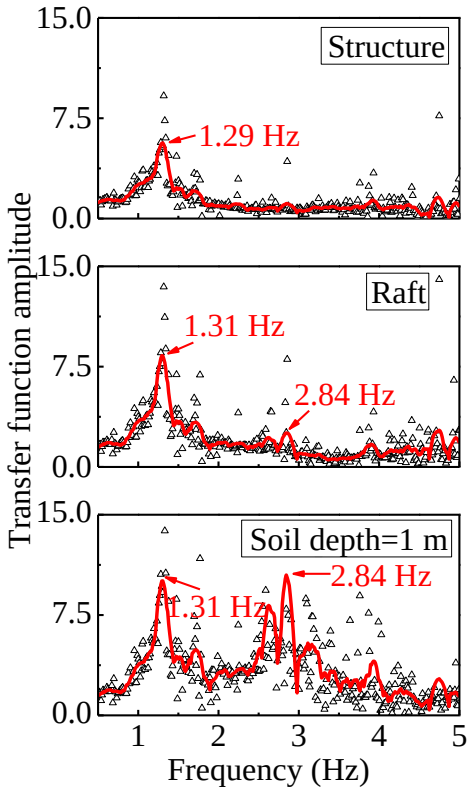

Figure 7 Transfer function under white noise excitation.

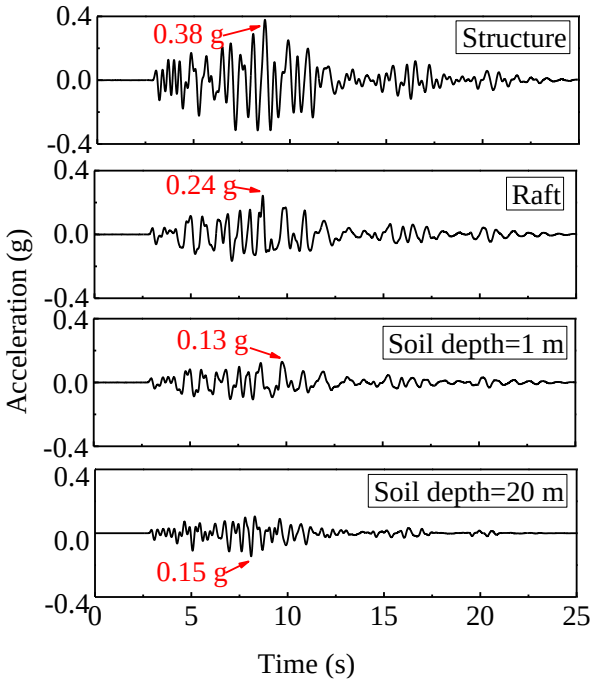

(a) Time history acceleration under the YG-0.1g wave

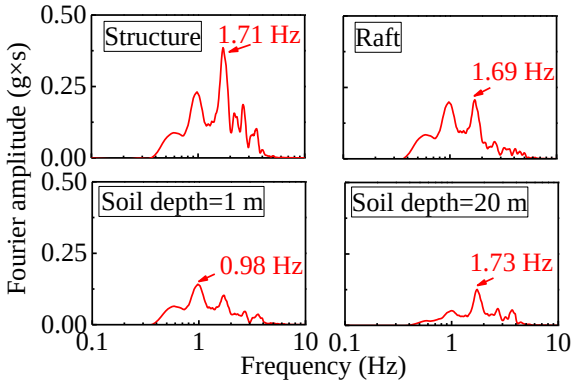

(b) Fourier amplitude under the YG-0.1g wave

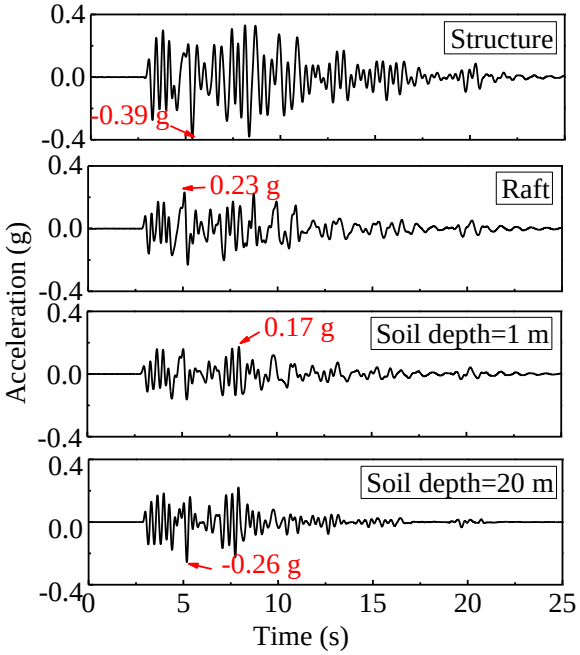

(c) Time history acceleration under the YG-0.2g wave

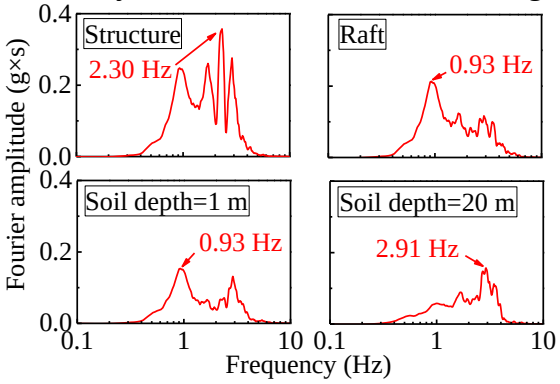

(d) Fourier amplitude under the YG-0.2g wave

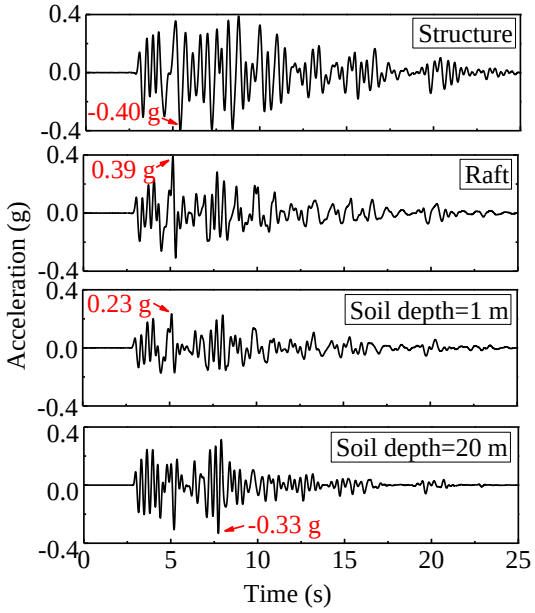

(e) Time history acceleration under the YG-0.3g wave

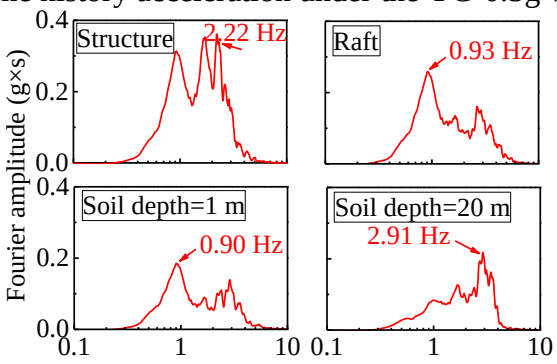

(f) Fourier amplitude under the YG-0.3g wave

Figure 8 Acceleration under YG wave excitation.

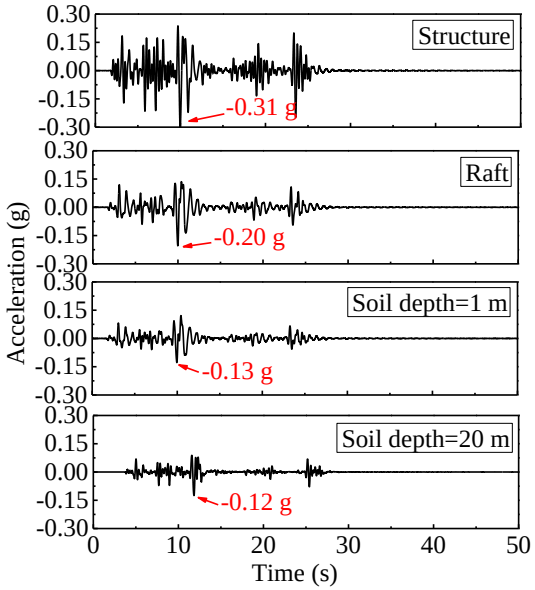

(a) Time history acceleration under the EL-0.1g wave

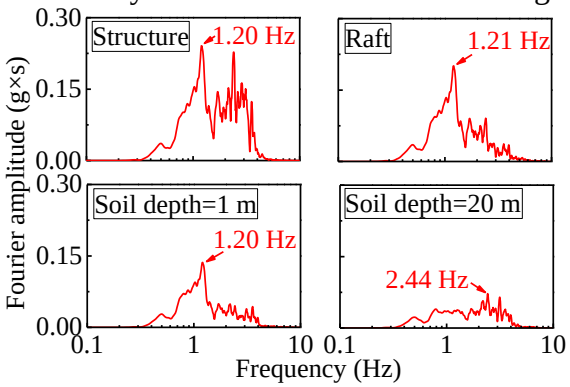

(b) Fourier amplitude under the EL-0.1g wave

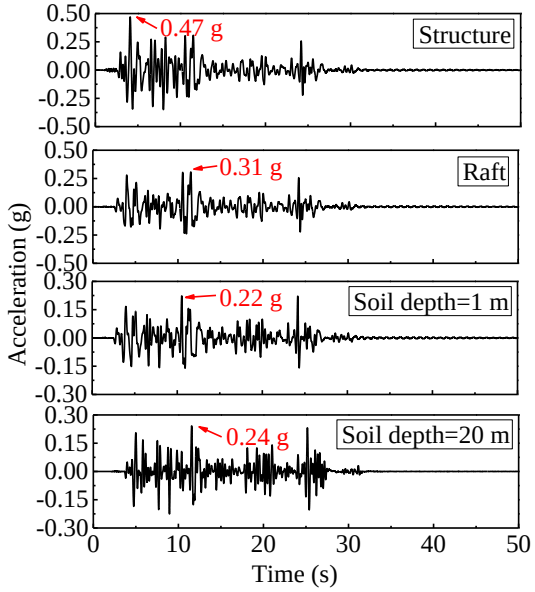

(c) Time history acceleration under the EL-0.2g wave

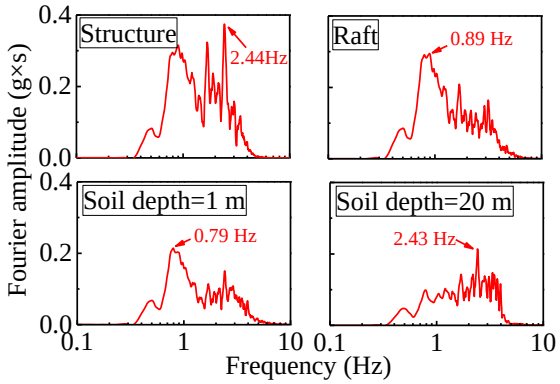

(d) Fourier amplitude under the EL-0.2g wave

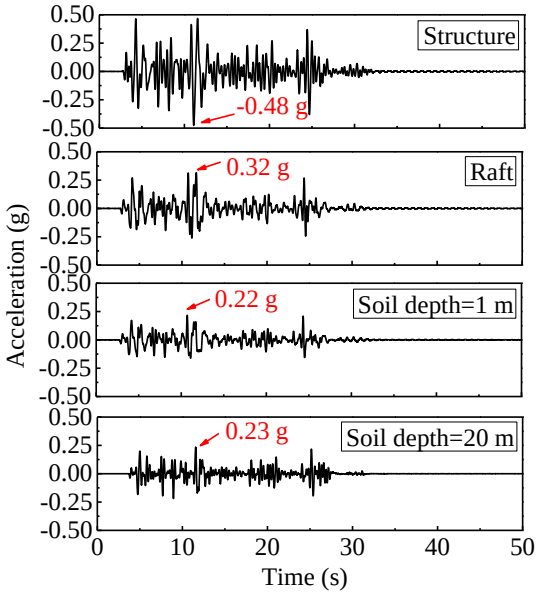

(e) Time history acceleration under the EL-0.3g wave

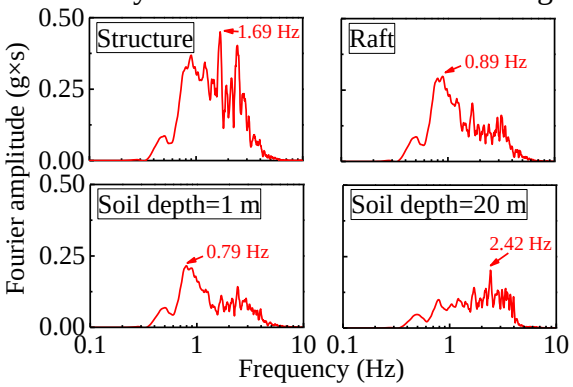

(f) Fourier amplitude under the EL-0.3g wave

Figure 9 Acceleration under EL wave excitation.

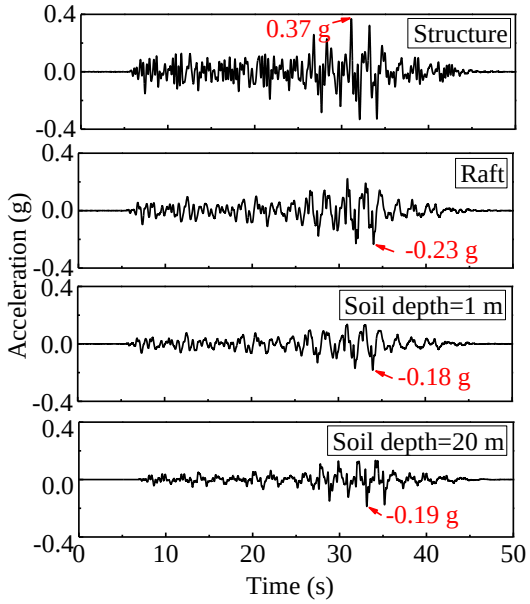

(a) Time history acceleration under the MEX-0.1g wave

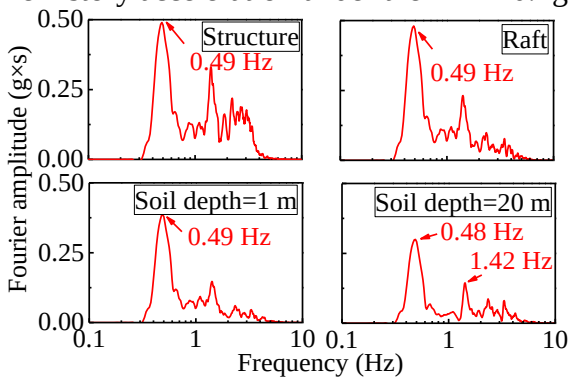

(b) Fourier amplitude under the MEX-0.1g wave

Figure 10 Acceleration under MEX wave excitation.

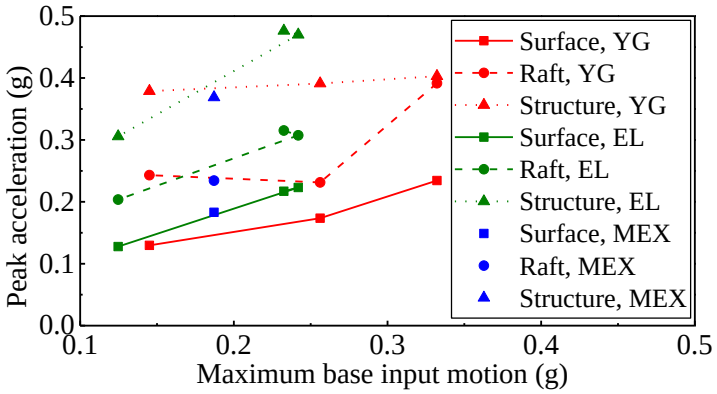

Figure 11 Peak superstructure acceleration.

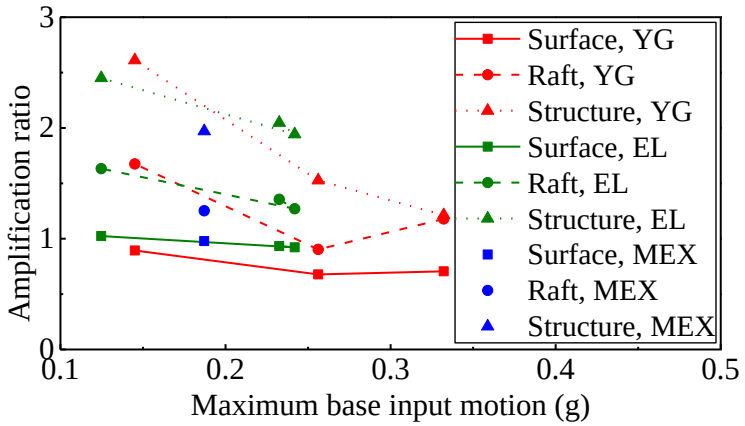

Figure 12 Amplification ratio for the peak acceleration.

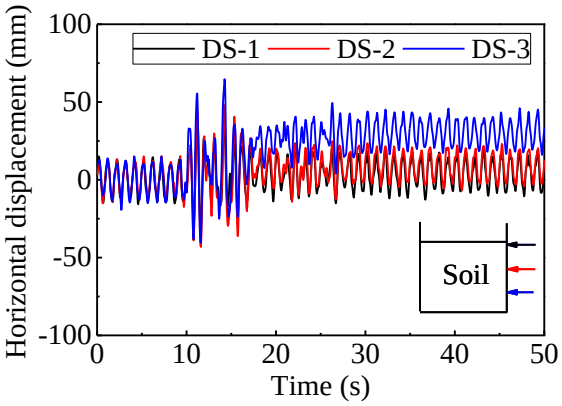

(a) Soil displacement under the YG-0.1g wave

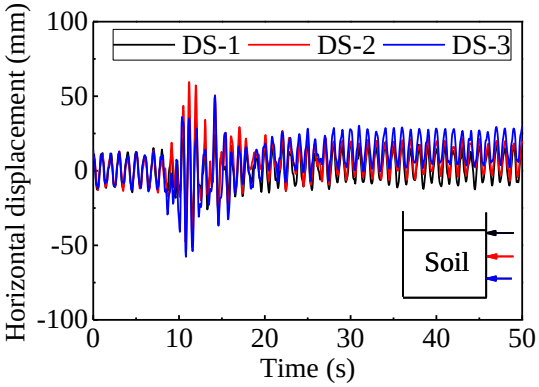

(b) Soil displacement under the YG-0.2g wave

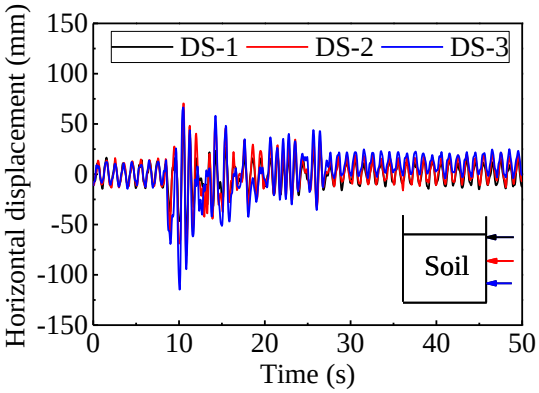

(c) Soil displacement under the YG-0.3g wave

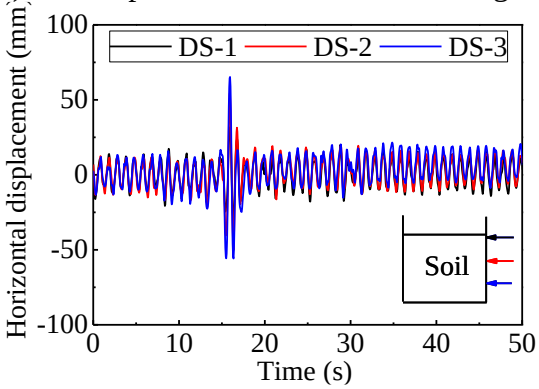

(d) Soil displacement under the EL-0.1g wave

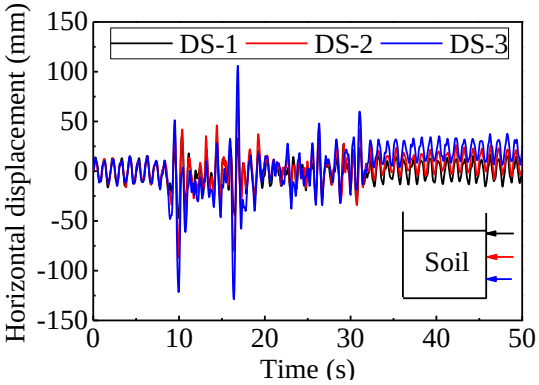

(e) Soil displacement under the EL-0.2g wave

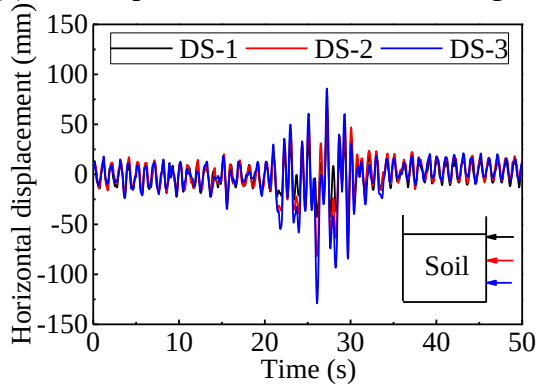

(f) Soil displacement under the EL-0.3g wave

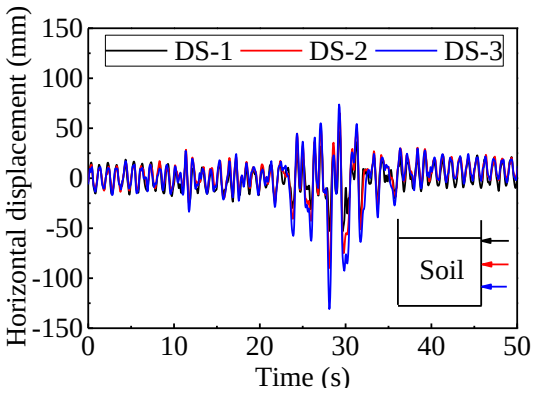

(d) Soil displacement under the MEX-0.1g wave

Figure 13 Horizontal displacement of soil for each of the considered excitation waves.

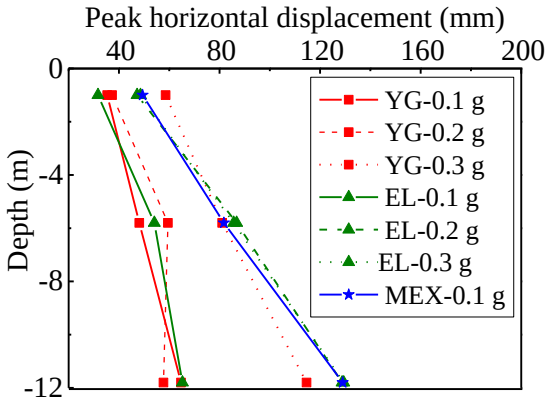

Figure 14 Peak horizontal displacement of soil.

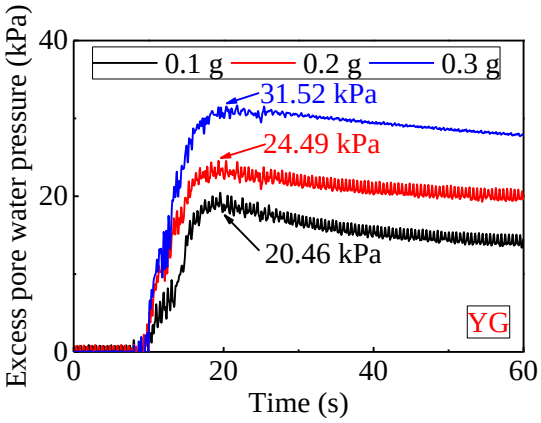

(a) Excess pore water pressure under the YG wave

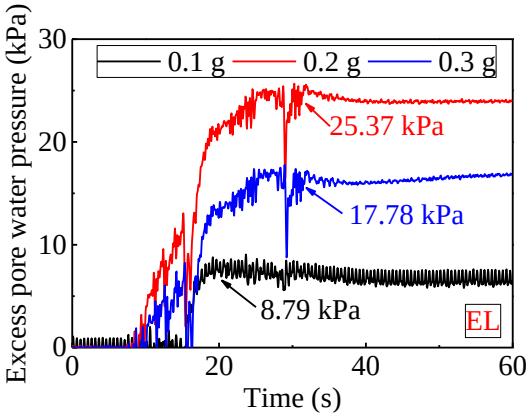

(b) Excess pore water pressure under the EL wave

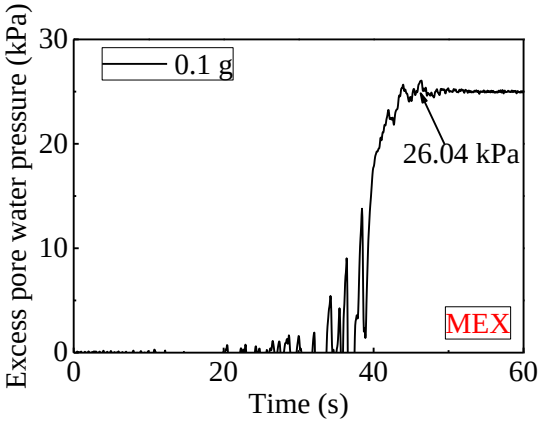

(c) Excess pore water pressure under the MEX wave

Figure 15 Excess pore water pressures under all considered earthquake wave excitations.

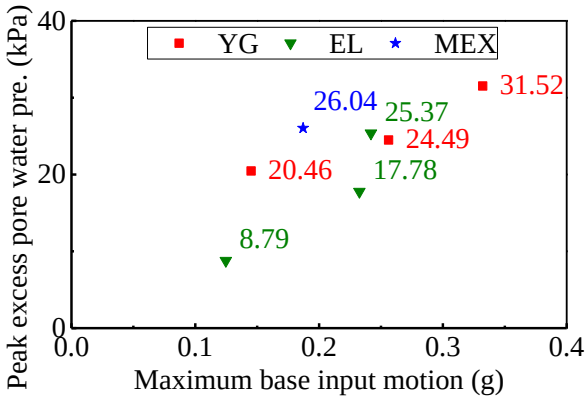

Figure 16 Peak instant excess pore water pressure.

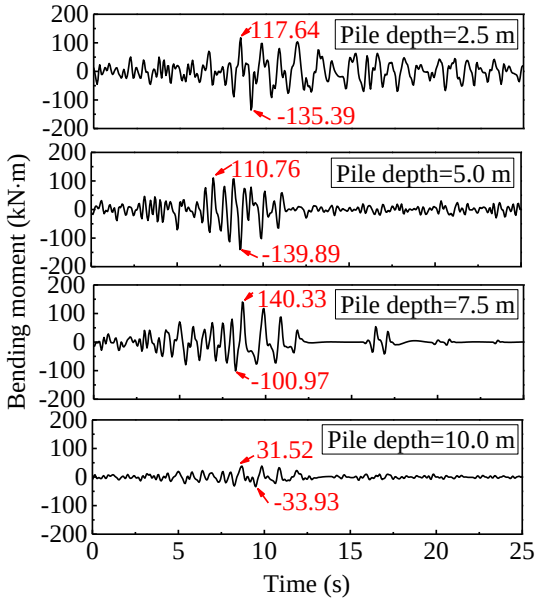

(a) Time history bending moments

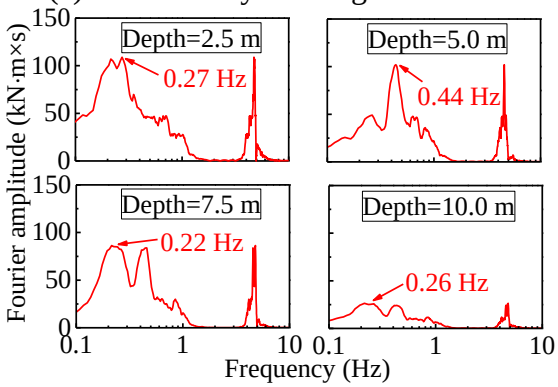

(b) Fourier amplification

Figure 17 Bending moment of pile 2 under YG-0.1 g wave excitation.

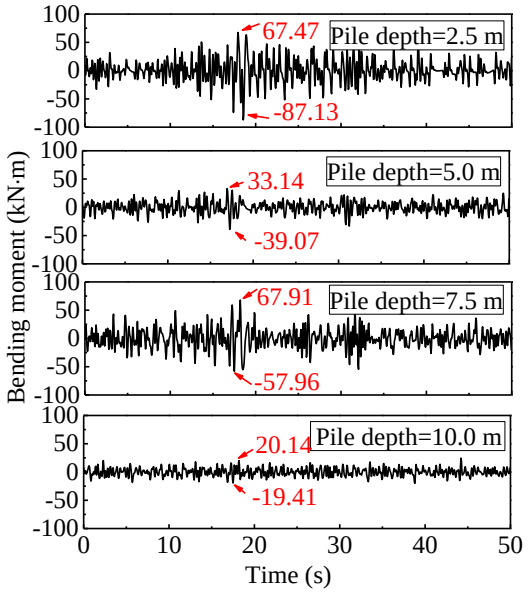

(a) Time history bending moments

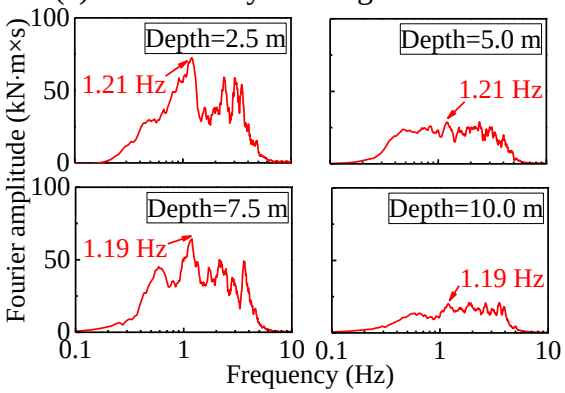

(b) Fourier amplification

Figure 18 Bending moment for pile 2 under EL-0.1 g wave excitation.

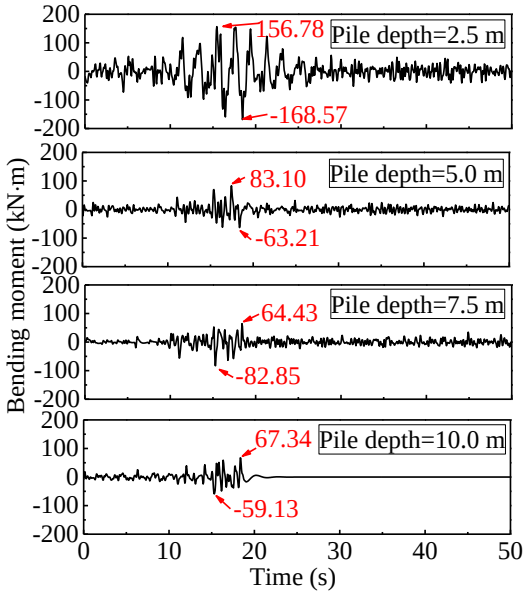

(a) Time history bending moments

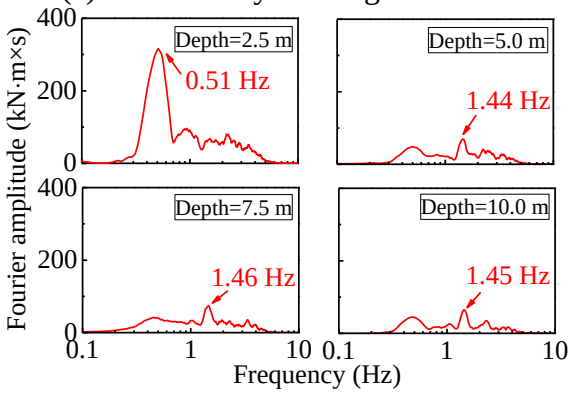

(b) Fourier amplification

Figure 19 Bending moment for pile 2 under MEX wave excitation.

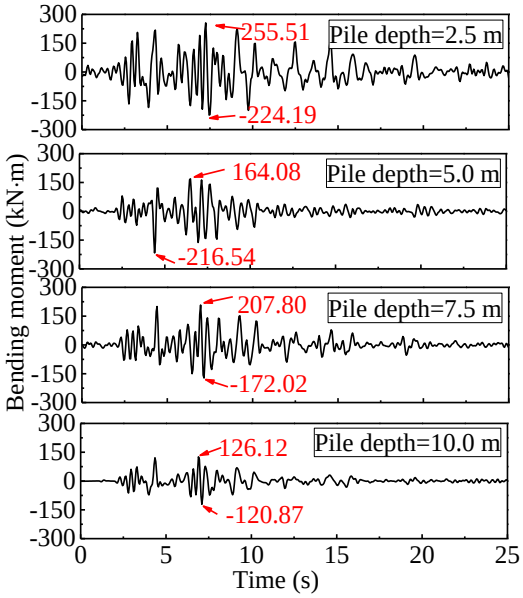

(a) Time history bending moments

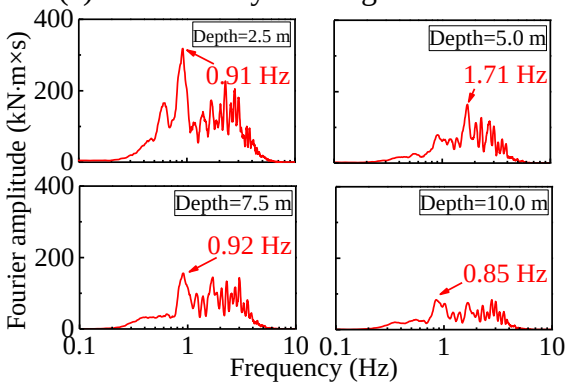

(b) Fourier amplification

Figure 20 Bending moment for pile 2 under YG-0.3 g excitation.

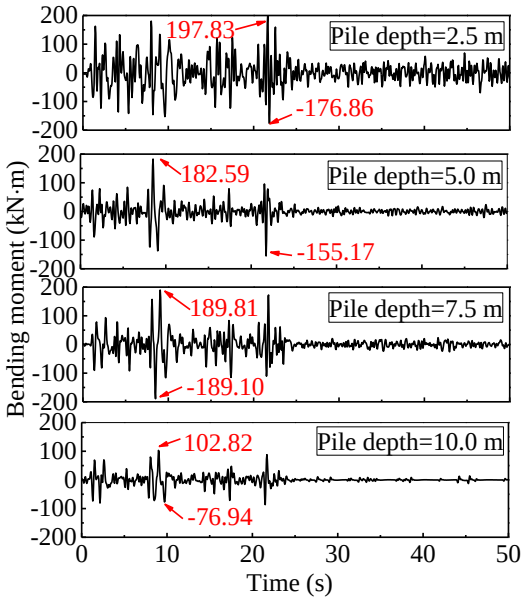

590
591 (a) Time history bending moments

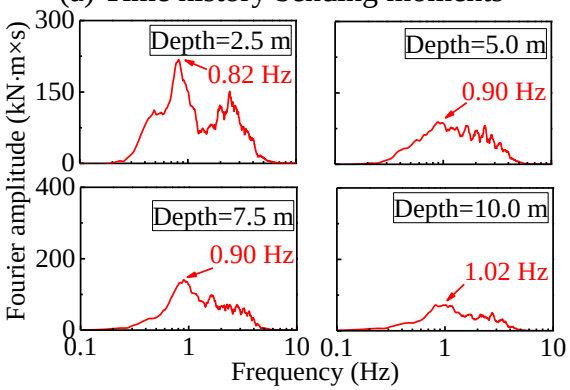

592
593 (b) Fourier amplification

594 Figure 21 Bending moment for pile 2 under EL-0.3 g wave excitation.

595

596

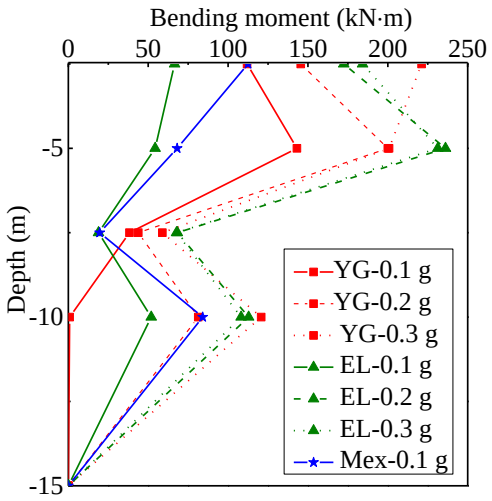

(a) P-1

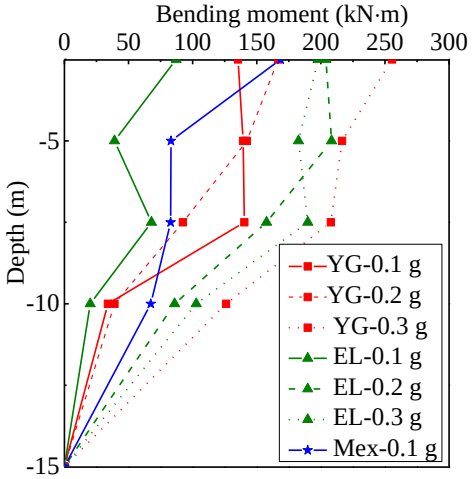

(b) P-2

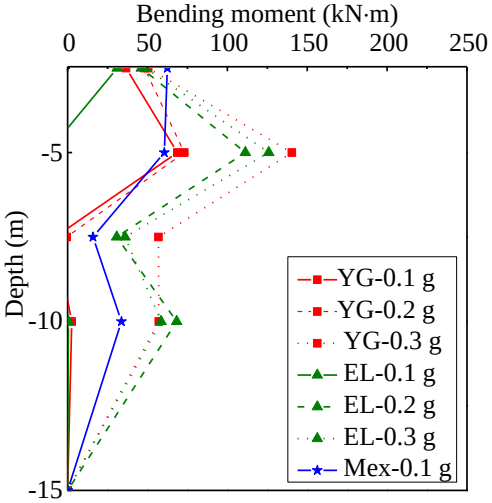

(c) P-3

Figure 22 Maximum bending moment for all piles.

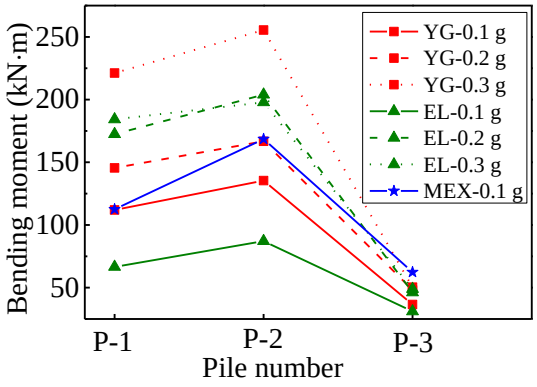

Figure 23 Maximum bending moment of the pile at depth of 2.5 m.

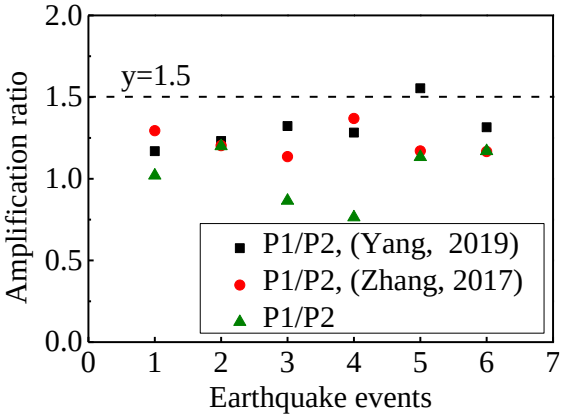

Figure 24 Ratio of maximum pile bending moment for P1/P2.

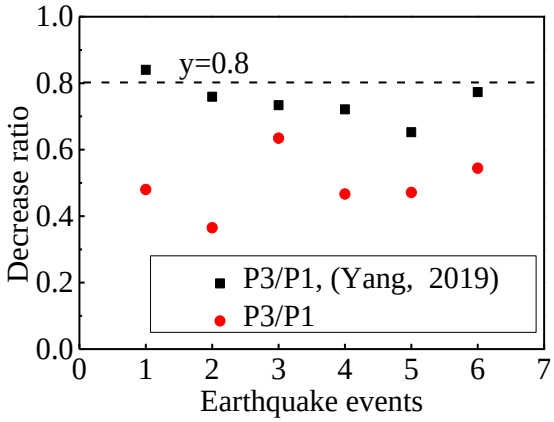

Figure 25 Ratio of maximum pile bending moment for P3/P1.

Figure captions

Tables

Table 1 Scaling laws for the dynamic centrifuge testing.

Parameter	Model/prototype	Dimensions
Length	1/50	L
Acceleration	50	LT^{-2}
Velocity	1	LT-1
Strain	1	$ML^{-1}T^{-2}$
Force	$1/50^2$	MLT^{-2}
Mass	$1/50^3$	M
Seepage velocity	50	LT^{-1}
Time (seepage)	$1/50^2$	T
Time (dynamic)	1/50	T
Force	$1/50^2$	MLT^{-2}

645

Table 2 Properties of the model and prototype.

Name	Properties	Model	Prototype
Pile	Diameter (m)	0.014	0.7
	Thickness	0.001	0.05
	Length (m)	0.3	15
	EI ($kN \cdot m^2$)	0.06072	379 498
Raft	Length (m)	0.238	11.9
	Width (m)	0.181	9.05
	Thickness (m)	0.016	0.8
Superstructure	Cuboid length (m)	0.221	11.05
	Cuboid width (m)	0.164	8.20
	Cuboid height (m)	0.074	3.70
	Cuboid thickness (m)	0.001	0.05
	Cylinder diameter (m)	0.108	5.40
	Cylinder height (m)	0.1218	6.09
	Cylinder thickness (m)	0.002	0.1
	Dome diameter (m)	0.108	5.40
	Dome height (m)	0.0224	1.12
	Dome thickness (m)	0.025	1.25

646

647

Table 3 Properties of the piles used in this and previous studies.

Pile type	Outer/thickness; m	Length; m	Flexural rigidity, EI; kN·m^2
Tube aluminium pile	0.7/0.05	15	379 498
Aluminium pile (Boulanger *et al*. 1999)	0.67	15	417 000
Solid aluminium (Zhang *et al*. 2017)	1	14	3 436 117
Tube aluminium pile (Yang *et al*. 2019)	0.5/0.014	10	1 270 000

652
653 Table 4 Basic properties of the Shanxi kaolin clay used in this study.

Property	Value
Particle Size; μm	10
Water content; %	24.55
Bulk unit weight; γ ;kN/m^3	23.63
Liquid limit, ω_L; %	31
Plastic limit, ω_P; %	20
Plastic Index, I_P; %	11

654 Note: The bulk unit weight was measured after the tests were complete.
655

656
657

Table 5 Dynamic centrifuge program.

Test identification	Wave	α_{max}; g	A_{max}; g
White wave	White	0.05	0.07
YG-0.1 g	YG	0.1	0.15
EL-0.1 g	EL	0.1	0.13
MEX-0.1 g	MEX	0.1	0.19
YG-0.2 g	YG	0.2	0.26
EL-0.2 g	EL	0.2	0.24
YG-0.3 g	YG	0.3	0.33
EL-0.3 g	EL	0.3	0.23

658
659

660 Table 6 Peak horizontal displacement of soils.

Test identification	DS-1; mm	DS-2; mm	DS-3; mm
YG-0.1 g	35.33	48.09	64.71
YG-0.2 g	37.29	59.49	57.73
YG-0.3 g	58.57	81.08	114.61
EL-0.1 g	31.67	54.09	65.27
EL-0.2 g	47.22	86.82	128.77
EL-0.3 g	48.57	85.65	129.40
Mex-0.1 g	49.42	81.75	128.99

661
662

663 Table 7 Vertical displacement and inclination of structure.

Case	LS1; mm	LS2; mm	Average settlement; mm	Inclination
YG-0.1 g	0.26	2.94	1.60	1/3508
YG-0.2 g	0.70	3.46	2.08	1/3413
YG-0.3 g	1.98	3.70	2.84	1/5463
EL-0.1 g	-1.64	3.30	0.83	1/1902
EL-0.2 g	3.61	3.08	3.35	1/17787
EL-0.3 g	-1.07	2.89	0.91	1/2375
Mex-0.1 g	2.54	0.09	1.32	1/3838

664
665

666 Table 8 Horizontal displacement of structure.

Case	Horizontal displacement; mm
YG-0.1 g	6.55
YG-0.2 g	8.89
YG-0.3 g	13.58
EL-0.1 g	7.43
EL-0.2 g	27.29
EL-0.3 g	25.11
Mex-0.1 g	-26.57

667
668

Table captions

Table 1 Scaling laws for the dynamic centrifuge testing.
Table 2 Properties of the model and prototype.
Table 3 Properties of the piles used in this and previous studies.
Table 4 Basic properties of the Shanxi kaolin clay used in this study.
Table 5 Dynamic centrifuge program.
Table 6 Peak horizontal displacement of soils.
Table 7 Vertical displacement and inclination of structure.
Table 8 Horizontal displacement of structure.